

Experimental exploration of the vector nature of the dynamic order parameter near dynamic magnetic phase transitions

M. Quintana,¹ E. Oblak,¹ J. M. Marín Ramírez,^{1,2} and A. Berger¹

¹*CIC nanoGUNE BRTA, E-20018 Donostia - San Sebastián, Spain*

²*Instituto de Física, Facultad de Ciencias Exactas y Naturales, Universidad de Antioquia, AA 1226, Medellín, Colombia*

 (Received 26 May 2020; revised 4 September 2020; accepted 8 September 2020; published 28 September 2020)

We have devised an experimental study to explore the vector nature of the dynamic order parameter \mathbf{Q} and the corresponding dynamic fluctuation σ^Q and susceptibility χ^Q tensors in the vicinity of the dynamic phase transition (DPT). For this purpose, we have fabricated epitaxial Co and CoRu thin films with (10 $\bar{1}$ 0) surface orientation and associated in-plane uniaxial anisotropy to mimic the behavior of an anisotropic Heisenberg model in the absence of magnetostatic interactions. Specifically, we measured the time-dependent magnetization component parallel to the externally applied magnetic field for different orientations of the magnetic easy axis (EA) while exploring the dynamic phase space defined by the applied oscillatory field amplitude H_0 and an additionally applied time-independent bias field H_b . The magnetization dynamics was hereby observed by utilizing an ultrasensitive transverse magneto-optical Kerr effect setup that allowed for real-time observations of the magnetic state evolution. Our experimental results demonstrate that while the position of the critical point changes upon rotating the EA away from the field axis, all qualitative aspects of the dynamic phase diagram close to the critical point are unchanged and the DPT can be universally observed. Also, metamagnetic anomalies occur for all measurement conditions. All our results are in agreement with a domain nucleation initiated magnetization reversal process and indicate that the overall dynamic state is dominated by the magnetization component parallel to the EA, so that a change in orientation in between the field axis and EA leads to a rather trivial rotation of the \mathbf{Q} vector, which simply follows the EA.

DOI: [10.1103/PhysRevB.102.094436](https://doi.org/10.1103/PhysRevB.102.094436)

I. INTRODUCTION

Dynamically ordered states and pattern formations are very relevant aspects of different branches of science [1]. Examples of such patterns in the physical sciences are laser emission [2], material defects [3,4], and the formation of sand dunes [5,6], to name a few. An even broader range of examples includes brain activity patterns [7], interactions between complex biological systems [8], and self-organized criticality [9]. In this context certain systems are known to undergo qualitative changes in their dynamic behavior at a specific critical value of an external control variable such as a field, leading to what is known as a dynamic phase transition (DPT). The understanding of this DPT phenomenon can provide very significant information about a system's collective dynamics, as well as relevant insights into nonequilibrium physics more generally, which is crucially important in many scientific fields.

DPTs are known to happen in ferromagnetic materials under specific conditions [10]. For temperatures below the Curie temperature T_C , the dynamic magnetization trajectory $M(t)$ can exhibit qualitative changes as an externally applied magnetic-field sequence $H(t)$ is modified. Usually in the framework of the DPT, a periodic magnetic field is considered, characterized by its period P and amplitude H_0 [11]. The dynamic magnetization response to such an oscillating field $H(t)$ now depends on an intrinsic time constant τ with which the spins collectively relax towards the thermodynamically stable

state at a given field strength [12]. If the period of the magnetic field is much larger than τ ($P \gg \tau$), the magnetic-field changes are slow enough so that the magnetization can follow the field sequence, even if there is a conventional magnetic hysteresis phase shift between $M(t)$ and $H(t)$, as shown in Fig. 1(a). Correspondingly, $M(H)$ will exhibit rather conventional hysteresis loops centered around a time-averaged zero magnetization value in this slow dynamic regime. If otherwise $P < \tau$, the field oscillations will be so fast that the magnetization cannot follow them and correspondingly, $M(t)$ will only show small oscillations around one of typically two sign-inverted nonzero remanent magnetization values. Figure 1(b) shows a field oscillation with $P < \tau$ and the two corresponding steady-state magnetization trajectories. In Figs. 1(a) and 1(b), the green dashed lines represent the field-cycle-averaged magnetization values Q defined as

$$Q = \frac{1}{P} \int_0^P M(t) dt. \quad (1)$$

In the slow dynamics case, i.e., Fig. 1(a), the magnetization oscillations lead to $Q = 0$. This is known as the dynamic paramagnetic (PM) state or phase. In the rapidly varying field case, i.e., Fig. 1(b), magnetization oscillations center around an average magnetization value $Q \neq 0$. This is known as the dynamic ferromagnetic (FM) state or phase, which furthermore has two separate dynamically stable solutions that have

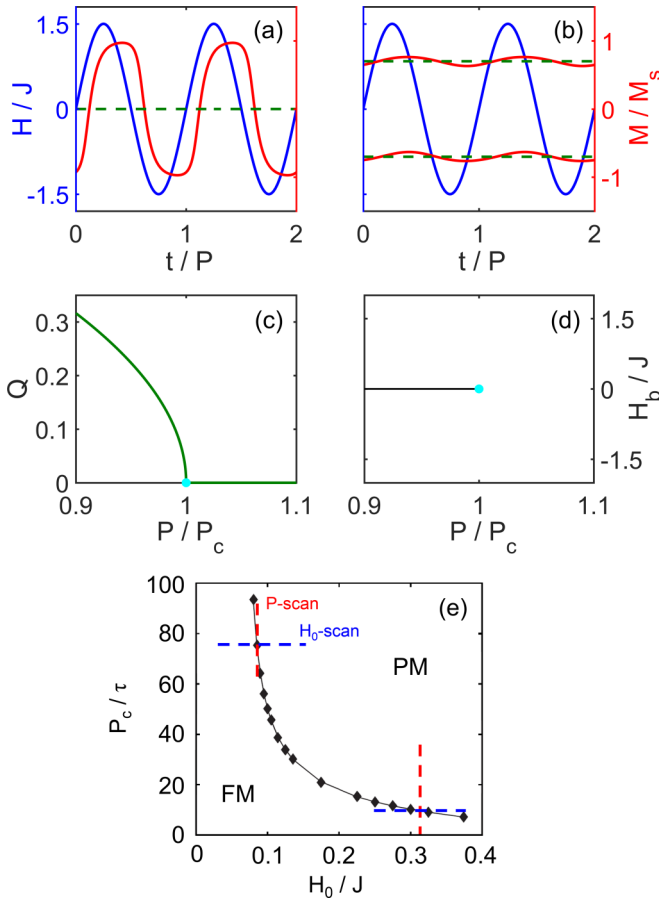


FIG. 1. (a), (b) Schematic examples of H vs t (blue) and M vs t (red) signals for two different periods in the dynamic PM phase (left) and FM phase (right), respectively. The horizontal dashed green lines indicate the cycle-averaged magnetization Q in each case. (c) Q vs P/P_c characteristic exhibiting a power-law dependency near the critical point at $P = P_c$, marked as a cyan dot. (d) Schematic nonequilibrium phase diagram of a dynamic magnetic system driven by a periodic magnetic field as a function of P/P_c and H_b . The horizontal black line at $H_b = 0$ and $P < P_c$ represents a phase boundary that is associated with a first-order dynamic phase transition. The cyan dot at $P = P_c$ and $H_b = 0$ represents the critical point at which a second-order dynamic phase transition occurs. (e) Characteristic behavior of the critical period P_c vs H_0 from [13]. The blue and red dashed lines represent the H_0 or P scans that can be utilized to explore the phase space.

a positive or negative average magnetization of equal magnitude. Figure 1(c) represents the transition from one dynamic state to the other as P varies for a constant H_0 value. The symmetry breaking from the dynamical FM to the dynamical PM phase happens at a unique critical period P_c , marked by the cyan dot in Fig. 1(c), and represents a nonequilibrium second-order phase transition, i.e., a DPT.

This DPT shares a lot of similarities with the usual equilibrium thermodynamic phase transition (TPT) of ferromagnets, which have been well described in the literature [13]. In both cases, there is an order parameter (M or Q) that undergoes a second-order phase transition when crossing a critical point (T_C or P_c , respectively). Furthermore, in theoretical studies Q has been found to follow a power-law description close to P_c

as shown in Fig. 1(c), namely,

$$Q(P \rightarrow P_c) \sim (P_c - P)^\beta. \quad (2)$$

It has been also observed in these theoretical studies comparing systems of the same universality class that the value of the critical exponent β for Q agrees with the value of the corresponding critical exponent in the equilibrium TPT, for which $M(T \rightarrow T_C) \sim (T_C - T)^\beta$ in the static ferromagnetic regime [14–17].

Further similarities between the DPT and TPT in magnetic systems are found when a constant bias field H_b is applied in addition to the field oscillations. This constant bias field has been identified as the conjugate field of the DPT order parameter for the case of a sinusoidal magnetic field [18–21], mimicking the effect of an external magnetic field in the thermodynamic equilibrium phase diagram. The bias field modifies the value of Q in both the FM and PM phases. Upon an inversion of H_b in the dynamic FM phase, Q shows a bistability regime close to the $H_b = 0$ field crossing point, followed by a discontinuous order-parameter change, which is associated with a first-order phase transition at exactly $H_b = 0$. In the dynamic PM phase, Q changes continuously as H_b varies. Figure 1(d) is a schematic representation of the phase diagram as a function of both P and H_b in which the first-order phase transition is represented as a black line and the already mentioned second-order DPT is visualized by means of a cyan dot. Further relevant parameters related to the dynamic order parameter Q are dynamic fluctuations σ^Q and susceptibility χ^Q , defined at every point of the P - H_b phase space except for the phase boundary itself as

$$\sigma^Q = \sqrt{\langle Q^2 \rangle - \langle Q \rangle^2}, \quad (3)$$

$$\chi^Q = \left. \frac{\partial Q}{\partial H_b} \right|_{P, H_0}. \quad (4)$$

Both fluctuations and susceptibility have been shown to exhibit anomalously sharp sidebands in the PM dynamic phase close to the critical point, known as metamagnetic anomalies [22,23]. These fluctuations correspond to very steep but still continuous changes in Q as H_b varies. The relevance of these metamagnetic anomalies is that they do not have an analog in the corresponding thermodynamic equilibrium phase diagram for conventional ferromagnets or spin models. Thus they constitute a significant difference between the collectively occurring dynamic magnetization reversal and the collective thermodynamic equilibrium in their respective paramagnetic regimes.

In many ferromagnetic systems, including Ising-like spin systems, the collective spin or magnetization reversal is triggered by an applied-field-assisted nucleation of inverted spin clusters and subsequent domain-wall propagations. These microscopic processes have been studied in detail in the past, including their relative significance and overall impact on hysteresis loops [24]. One direct consequence of these microscopic reversal processes in terms of the resulting collective behavior is that P_c is strongly dependent on the field amplitudes used for the observation of the DPT, leading to a $P_c \sim \exp(1/H_0)$ dependency that is clearly visible in Fig. 1(e) [13,14,23]. This dependence shifts the critical point towards smaller P values as H_0 increases, and it allows one to explore

the phase space near the FM/PM phase line in two different ways. One is the usual P scan, shown via exemplary red dashed lines in Fig. 1(e), in which P varies while H_0 is held constant. The other way is the H_0 scan, shown by means of representative blue dashed lines, in which H_0 varies for a constant P . For slower critical dynamics, i.e., higher P_c values in Fig. 1(e), the H_0 scan allows for a wider exploration of the relevant phase space near the DPT phase line, because in this regime P_c decreases very strongly as a function of H_0 . Conversely, for faster critical dynamics, i.e., smaller values of P_c in Fig. 1(e), the P scan is a more suitable methodology, given that in this regime P_c is not so strongly dependent on the H_0 values that are used to generate the dynamic magnetic state.

Theoretically, DPTs have been most widely studied in the context of the kinetic Ising model (KIM), which considers one-dimensional spin variables S_i located on lattice sites i and interacting with each other via a ferromagnetic exchange energy constant J and the time-dependent external magnetic field $H(t)$ by means of a conventional Zeeman energy term, resulting in the Hamiltonian

$$\mathcal{H} = -J \sum_{[i,j]} S_i S_j - H(t) \sum_i S_i. \quad (5)$$

In this expression, the brackets refer to the sum over nearest neighbors. In spite of its simplicity, the KIM has enabled very detailed studies regarding the DPT in the context of both Monte Carlo simulations [14,15,17,18,23,25,26] and mean-field approximations [10,19,20,27], which allowed for an understanding of many relevant aspects of DPTs. Rather few theoretical studies have analyzed DPTs in the context of Heisenberg models [28,29], which generally offer greater comparability with experimental systems, given that magnetic anisotropies are typically very small for most material systems if compared to the exchange energy, and thus the true nature of three-dimensional spin variables is far better represented. Experimentally, a number of studies analyzed magnetization dynamics for different experimental systems decades ago [30–32], but these studies failed to address the occurrence of the DPT and the actual measurement of the order parameter Q . These aspects, which are actually needed to achieve an unambiguous characterization of the macroscopic dynamic state, were for the first time experimentally addressed in an investigation of Co/Pt multilayers [33]. However, only later studies on in-plane magnetized uniaxial Co films managed to map the phase diagram properly, providing conclusive evidence that H_b is the conjugate field and demonstrating that the phase line according to Fig. 1(d) actually exists [34]. More recently, our group also demonstrated the already mentioned metamagnetic anomalies [22] in the same type of material system before these anomalies were theoretically confirmed by means of Monte Carlo simulations [23].

In spite of these many different works and approaches, the vector nature of magnetization \mathbf{M} , and thus the potential relevance of Q being a vector quantity, has been ignored in all experimental works and nearly all theoretical works. Even the few theoretical works that investigated DPTs in the context of Heisenberg-type models [28,29] have not addressed the influence of a bias field on the system's dynamic state, and thus no

relevant exploration of the overall phase space or an analysis of the existence of metamagnetic anomalies under different conditions has been done, neither experimentally nor theoretically. Thus virtually nothing is known about Q as a vector quantity and its impact onto the dynamic phase diagram and dynamic phase transitions. Given the vector nature of \mathbf{M} , even the definition of Q in Eq. (1) is insufficient because it does not consider the three-dimensional character of magnetization $\mathbf{M} = (M_x, M_y, M_z)$. Correspondingly, we need to first generalize the dynamic order parameter as a three-dimensional quantity $\mathbf{Q} = (Q_x, Q_y, Q_z)$, which is defined as

$$\mathbf{Q} = \frac{1}{P} \int_0^P \mathbf{M}(t) dt. \quad (6)$$

Correspondingly, now fluctuations σ^Q and susceptibility χ^Q become tensorial quantities σ^Q and χ^Q , whose components are defined as

$$\sigma_{ij}^Q = \sqrt{\langle Q_i Q_j \rangle - \langle Q_i \rangle \langle Q_j \rangle}, \quad (7)$$

$$\chi_{ij}^Q = \frac{\partial Q_i}{\partial H_b j}. \quad (8)$$

Here, i and j represent the three Cartesian coordinates. In the following we will define the \mathbf{H} axis as the z axis for reasons of transparency, i.e., $\mathbf{H} = H(t)(0, 0, 1)$.

Given the above-mentioned complete lack of knowledge about the vectorial properties of Q as the relevant macroscopic dynamic order parameter, the core goal of this work is to make an initial attempt to experimentally analyze the vector nature of Q close to the DPT. More specifically, we will investigate the overall phase space near the DPT by exploring the anisotropic nature of specifically designed samples that mimic the anisotropic Heisenberg model, for which one can expect the dynamic response to depend on the relative alignment in between the applied field direction and the preferred magnetization axis. Correspondingly, we will study the dynamic order parameter as well as dynamic fluctuations and susceptibility near the DPT, and by doing so explore if and how these quantities are impacted by the applied field orientation. This should allow us to determine whether the true vectorial nature of Q has a substantial quantitative or even qualitative impact on the collective dynamic phase diagram of magnetic films.

In the second section of this work, we introduce the experimental aspects utilized for this study. This includes specific properties of our samples related to their suitability for our study here, as well as core details of our transverse magneto-optical Kerr effect (T-MOKE) tool that allowed for a very precise experimental determination of dynamic magnetic states throughout the relevant phase space. In the third and main section we explore and discuss key experimental results that we obtained for selected samples. Finally, in the fourth and last section we draw general conclusions based upon our experimental results and give an outlook and perspective on the vectorial nature of Q and its relevance to understanding dynamic magnetic phases and phase transitions in magnetic films.

II. EXPERIMENTAL ASPECTS

As described in the previous section, the DPT was initially predicted and subsequently theoretically investigated for Ising-type spin systems that exhibit exchange interactions, while magnetostatic interactions were simply not considered. In order to experimentally explore the properties of an Ising-type model, one should pick a ferromagnetic material with uniaxial anisotropy so that only two stable magnetization states exist at zero field. However, in real materials magnetic properties are more realistically represented by anisotropic Heisenberg models, given that the anisotropy energy is typically very small compared to the exchange energy, and thus field-induced reorientations of magnetic moments into the hard axis are possible. Nonetheless, in relation to fundamental aspects of ferromagnetism, such as the critical exponents of the TPT, the anisotropic Heisenberg model mimics the behavior of the Ising model [35], and therefore the choice of this type of sample is a reasonable approach. In order to achieve the near suppression of magnetostatic interactions experimentally, one has to choose a geometry, in which the magnetostatic energy is very small. This can be done by choosing samples with thin-film geometry and an easy axis (EA) within the surface plane of the film. Indeed, the viability of this strategy has already been verified in our prior work for Co [22,34,36] and CoRu thin films [37–39].

Following this previously used strategy, we have fabricated thin-film samples of $\text{Co}_{100-x}\text{Ru}_x$ alloys for our study that were epitaxially grown with the required (10 $\bar{1}$ 0) crystallographic orientation. Here, x stands for the Ru concentration in atomic percent within the magnetic layer. These alloys have in-plane uniaxial anisotropy with the EA being parallel to the crystallographic c axis, which is oriented in the surface plane and thus allows for detailed investigations of dynamic magnetic-field responses. The choice of the specific Ru content utilized here comes from the fact that T_C decreases almost linearly with x [37]. By growing samples with different Ru concentrations, we can explore the vectorial nature of \mathbf{Q} in the phase space near the DPT for different T/T_C ratios, even if all measurements are limited to T being room temperature. This is potentially very relevant, because the T/T_C dependence of the DPT could be very substantial, and some prior theoretical work even predicted a change in the order of the phase transition from second to first order as T/T_C is varied [10]. Similarly, the vectorial aspects of \mathbf{Q} could be relevantly impacted by changing T/T_C , an aspect that has not been explored in the scientific literature, neither experimentally nor theoretically. Only very recently have we been able to experimentally investigate the role that T/T_C has on the DPT, and we found substantial quantitative changes being induced by changing T/T_C , with the magnitude of metamagnetic anomalies becoming increasingly large as T_C approaches T [39]. However, in that work we focused exclusively on the easy axis M and Q , and thus did not explore the vector character of \mathbf{Q} , which is the topic of the present work. Nonetheless, here we decided to also study samples with different T/T_C ratios so that we might be in a position to observe relevant changes of the vectorial \mathbf{Q} or tensorial σ^ϱ and χ^ϱ quantities with T/T_C .

In this work, we focus on two different material concentrations, namely, $x = 0\%$ and $x = 18\%$, which we refer to as

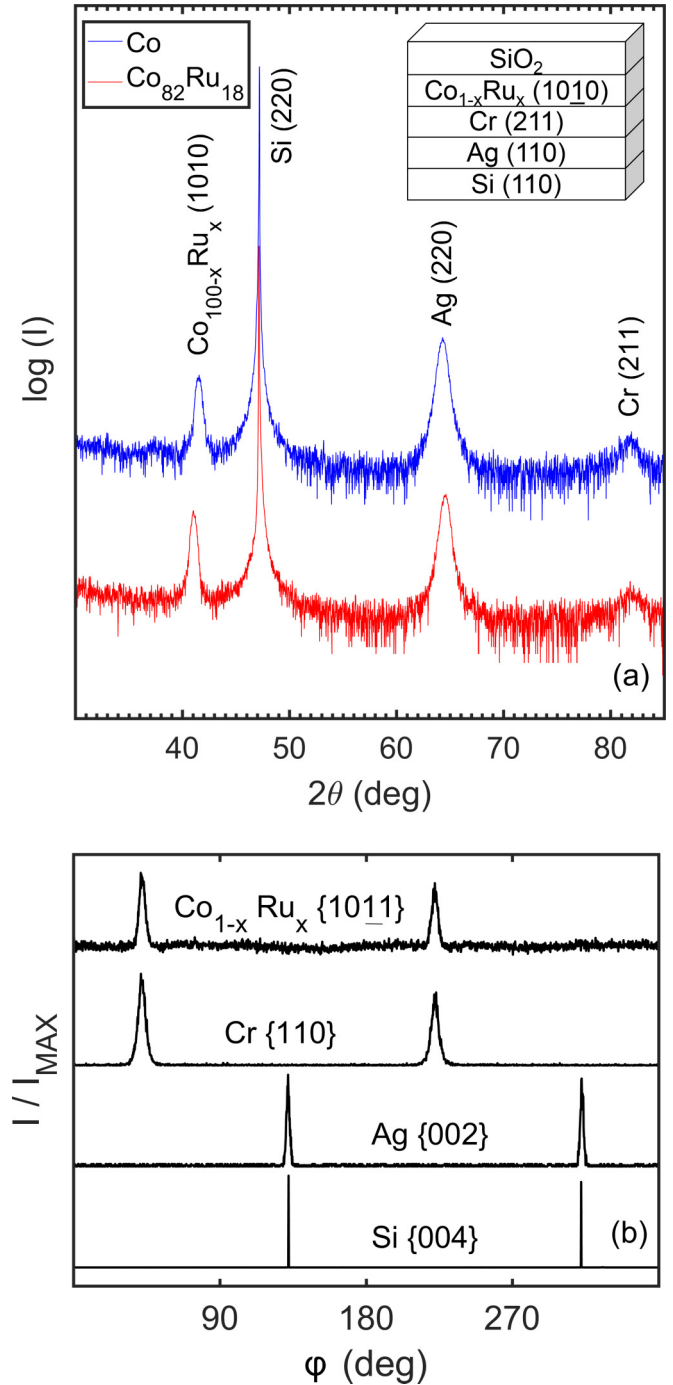


FIG. 2. (a) θ - 2θ -scan x-ray diffraction intensities for two different epitaxial $\text{Co}_{100-x}\text{Ru}_x$ samples, specifically, $x = 0$ (blue) and $x = 18$ (red). The epitaxial growth sequence is schematically shown as an inset in the figure. (b) Representative XRD φ scans of the 2θ poles of Si {004}, Ag {002}, Cr {110}, and $\text{Co}_{100-x}\text{Ru}_x$ {10 $\bar{1}$ 1} for the $\text{Co}_{82}\text{Ru}_{18}$ sample.

Co and $\text{Co}_{82}\text{Ru}_{18}$, respectively. These samples were epitaxially grown at room temperature using a commercial sputter deposition system. A specific growth sequence is required in order to promote the correct epitaxial orientation needed for our films [36,37]. The growth sequence is presented schematically as an inset in Fig. 2(a). We employed Si substrates with

(110) orientation. The native oxide was removed by using wet fluoric acid (HF). On top of the HF-etched Si (110) surface, a sequence of Ag (220) and Cr (211) layers, being 37.5 and 10 nm thick, respectively, are grown to generate a suitable template for the epitaxial growth of (hcp) Co (10 $\bar{1}$ 0) and CoRu (10 $\bar{1}$ 0) [40]. The ferromagnetic Co and CoRu layers that were fabricated for this study are 20 nm thick. On top of the magnetic films, a 10-nm-thick SiO₂ overcoat was deposited via RF sputtering to prevent oxidation of the samples. In [37], a CrRu layer was added to the epitaxial sequence between the Cr and CoRu sublayers to keep the quality of the epitaxial growth of the CoRu alloy film constant for different Ru concentrations for the purpose of enabling a precise comparative study of anisotropy constants. Here, we did not utilize this additional CrRu layer, because good epitaxial growth of the CoRu layer was achieved by directly growing it on top of the Cr (211) layer, even if the mismatch of the lattice constants changes slightly with Ru concentration. The Curie temperatures of our films were determined to be $T_C = 1400 \pm 80$ K for the case of the Co sample and $T_C = 700 \pm 30$ K for the case the Co₈₂Ru₁₈ sample [37,38]. This means that the T/T_C ratios of our measurements are approximately 0.21 and 0.43 for the Co and Co₈₂Ru₁₈ samples, respectively.

X-ray diffraction (XRD) measurements were carried out to verify the epitaxial nature and the crystallographic quality of our samples. In Fig. 2(a), we show typical XRD θ - 2θ measurement data for both samples. In these curves one observes the diffraction peaks corresponding only to the Co_{100-x}Ru_x (10 $\bar{1}$ 0), Si (220), Ag (220), and Cr (211) sublayers, corroborating the intended epitaxial stacking of our multilayered films as well as the absence of other crystallographic orientations. The SiO₂ layer grows amorphous and does not show any peak. We also performed XRD φ scans in order to obtain information about the in-plane alignment of the crystal structures and to verify their epitaxial relationship. In Fig. 2(b), we present representative scans for the Co₈₂Ru₁₈ (10 $\bar{1}$ 0) sample at four different crystal planes that are not parallel to the film surface. Data for the pure Co sample look virtually identical. All φ scans show two well-defined peaks that are 180° apart and whose positions match the stereographic projections of the nominal epitaxial structure [40]. The 90° shift between the Ag {002} and the Cr{110} peaks indicates that the Cr [1 $\bar{1}$ 0] crystallographic direction is parallel to the [001] direction of Ag and Si. The CoRu peaks appear at the same position as the Cr ones, indicating that CoRu [0001] and Cr [1 $\bar{1}$ 0] are parallel to each other, which verifies the intended epitaxial structure of the films.

The in-plane uniaxial magnetic anisotropy of our samples is verified by means of vibrating sample magnetometry (VSM) measurements. Specifically, we measured the magnetization component M_z parallel to the direction of the external field \mathbf{H} along the z axis. A schematic representation of the sample and field geometry is shown in Fig. 3(a). In Figs. 3(b) and 3(c), we show the measured remanent magnetization M_r normalized to its saturation value M_s as a function of the angle φ between the EA and the applied field direction for the Co and Co₈₂Ru₁₈ samples, respectively. These data are determined in zero field after first applying a magnetic field that is large enough to completely saturate the magnetization in any given direction and subsequently removing the field.

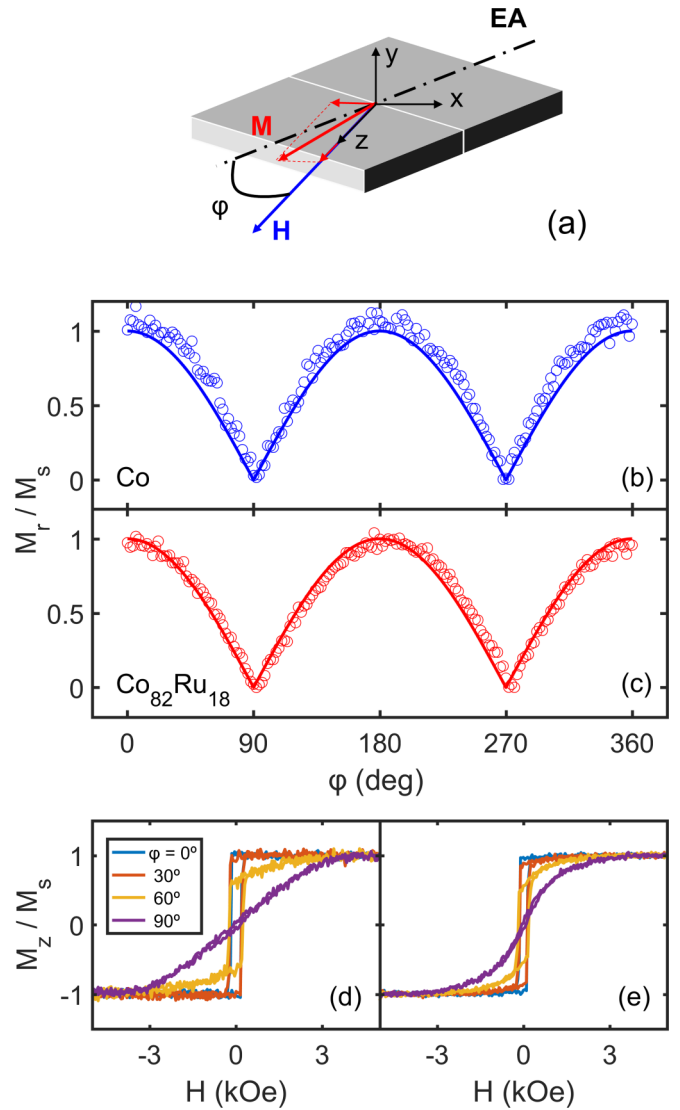


FIG. 3. (a) Schematic representation of the sample geometry indicating the relation in between the in-plane EA of magnetization, the direction of the applied field \mathbf{H} , and the in-plane magnetization \mathbf{M} exhibiting components M_z and M_x . (b), (c) Normalized remanent magnetization M_r/M_s vs φ after prior saturation along the z axis, measured at room temperature for the Co and Co₈₂Ru₁₈ samples, respectively. The symbols are the experimental magnetometry data, while the solid lines represent the ideal textbook behavior of a ferromagnet with uniaxial anisotropy. (d), (e) Hysteresis loop measurements at room temperature for the Co and Co₈₂Ru₁₈ samples, respectively, at selected sample orientations, represented by the corresponding φ values.

Both samples exhibit the expected angular dependence of M_r/M_s vs φ for a uniaxial magnetic system, including a 180° periodicity. Along the EA ($\varphi = 0^\circ$ and $\varphi = 180^\circ$), M_r/M_s is almost exactly 1, and its value decreases towards zero in a sinusoidal fashion as the sample is rotated towards the hard axis (HA) ($\varphi = 90^\circ$ and $\varphi = 270^\circ$). To illustrate the excellent agreement with the ideal textbook model of a ferromagnet with uniaxial anisotropy [41], we also plotted its behavior as continuous lines in Figs. 3(b) and 3(c) as a reference. These measurements also corroborate that magnetostatic effects are

indeed very weak in our samples and do not modify the static magnetic behavior in any significant way.

To further illustrate our samples' magnetic response, several hysteresis loops for different values of φ are displayed in Figs. 3(d) and 3(e) for the Co and $\text{Co}_{82}\text{Ru}_{18}$ samples, respectively. In both cases, along the EA the hysteresis loop shows an abrupt magnetization switch only, leading to a squarelike hysteresis loop appearance. For other values of φ , one can observe a weak bending of the loops before an abrupt magnetization switching occurs. This bending is not so relevant for small values of φ but becomes increasingly large as φ increases until, along the HA, magnetization reversal happens in a continuous fashion only. This specific feature in the hysteresis loops comes from the fact that when the EA is not aligned with the direction of the field, the resulting direction of magnetization is defined by an interplay between the anisotropy energy and the Zeeman energy, leading to an alignment of the magnetization along the EA for sufficiently low field strengths. We also observe from the data here that the anisotropy field H_k is larger than 2 kOe for both samples. Moreover, we see that the switching field, at which the large discontinuous reversal happens, is much smaller than H_k due to the existence of thermal excitations and the associated occurrence of domain nucleation within our samples, which triggers reversal processes and ultimately, the dynamic magnetic state that is associated with the DPT [42].

Consequently, our structural and static magnetic characterization data demonstrate that the specific growth sequence and material selection that we have chosen here are suitable to accomplish the fabrication of samples with in-plane uniaxial anisotropy that furthermore mimic the magnetization response of an anisotropic Heisenberg ferromagnet. These are exactly the aforementioned criteria for the experimental observation of the DPT. Furthermore, the M vs H curves in Figs. 3(d) and 3(e) reveal that sharp system-wide reversals occur, at least in a significantly broad φ range, which is another requirement for the observation and study of the DPT.

Due to its excellent sensitivity for thin-film samples, we have employed a magneto-optical Kerr effect (MOKE) setup to measure the dynamic state of our samples [43–50]. Our particular setup measures the magneto-optically induced ellipticity changes in the reflected light that are proportional to the transversal magnetization component along the applied field direction, i.e., M_z . A schematic representation of our setup is shown in Fig. 4(a). This particular configuration has been shown to increase the signal-to-noise ratio with respect to conventional T-MOKE setups more than 30-fold and is thus particularly suitable for our experimental study of dynamic magnetization behavior [51,52]. In our setup, an ultra-low-noise laser with $\lambda = 635$ nm and output power of 5 mW is utilized. The incident beam is aligned at an angle-of-incidence of 60° with respect to the surface normal. It passes first through a polarizer P_1 , which produces linearly polarized light, with the linear polarization being oriented at 45° with respect to the plane of incidence. The light is subsequently reflected by the sample, which is positioned inside the gap of an electromagnet. After reflection it passes through a quarter wave plate QWP and a second polarizer P_2 , after which it is detected by a photodetector. Both QWP and P_2 are aligned in such a way that we achieve large light intensity changes

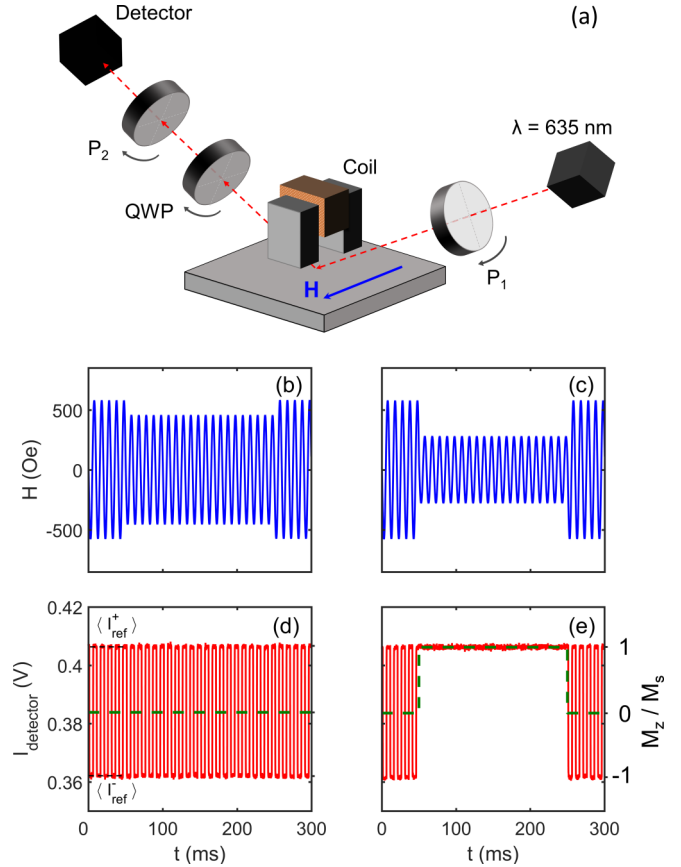


FIG. 4. (a) Experimental T-MOKE setup detection scheme consisting of a coherent light source with $\lambda = 635$ nm, an initial polarizer P_1 , a quarter wave plate QWP, a second polarizer P_2 , and a photodetector. The U-shaped electromagnet is located above the sample and produces a magnetic field H parallel to the sample surface at the point of the laser light spot. (b), (c) Experimental H vs t data consisting of five reference periods with an amplitude of $H_{\text{ref}} = 581$ Oe at the beginning and end of each sequence, and 20 cycles with $H_0 = 457$ Oe and $H_0 = 281$ Oe, respectively. (d), (e) T-MOKE intensity signals synchronously measured for the magnetic-field sequences in (b) and (c), respectively, for a $\text{Co}_{82}\text{Ru}_{18}$ sample using $\varphi = 0^\circ$. Green dashed lines stand for the average intensity in each period. $\langle I_{\text{ref}}^+ \rangle$ and $\langle I_{\text{ref}}^- \rangle$, represented as black dashed lines on the left-hand side of (d), correspond to the experimental intensity values used for the derivation of the M_z/M_s scale. The M_z/M_s axis is shown on the right-hand side of (e) and applies to (d) and (e).

at the detector and accordingly, optimal signal-to-noise ratios upon inversion of the magnetization state for our samples. It is worth emphasizing here that the detected signal in our setup is not affected by changes in the polar and longitudinal component of magnetization. Further details of our specific MOKE detection approach have been documented in [51]. For our study here, it is important to notice that our setup allows us to rotate the sample in such a way that we can align the EA away from the z axis in a precise, stable, and reproducible manner.

As with any magneto-optical measurement of hysteresis loop behavior, our measurements here do not directly access magnetization values, but instead we measure a quantity proportional to the magnetization component along the z axis,

which is also the field direction. Thus our experimental data have to be calibrated with respect to the signal values that are measured in saturation to allow for a relative magnetization calibration. Figures 4(b)–4(e) show several exemplary data sets associated with our calibration measurements for the $\text{Co}_{82}\text{Ru}_{18}$ sample in which the EA and the applied field are parallel to each other ($\varphi = 0^\circ$). Figures 4(b) and 4(c) show two examples of applied magnetic-field sequences versus time and Figs. 4(d) and 4(e) the corresponding time evolution of the photodetector voltage, which is proportional to the light intensity. In these calibration measurements we apply sinusoidal magnetic fields of different amplitudes using a fixed period of $P = 10$ ms. The first and the last five oscillations in both Figs. 4(b) and 4(c) are magnetic-field reference sequences with an amplitude $H_{\text{ref}} = 581$ Oe. The corresponding light intensity signals measured in these segments [Figs. 4(d) and 4(e)] show a time-dependent squarelike behavior, because H_{ref} is large enough to completely reverse the magnetization and induce a saturated magnetization state in either field direction (for this $\varphi = 0^\circ$ case). Correspondingly, the values of intensity measured at these points allow us to define the quantities $\langle I_{\text{ref}}^- \rangle$ and $\langle I_{\text{ref}}^+ \rangle$ [shown in Fig. 4(d)] that correspond to the negatively and positively saturated magnetization states, respectively, based upon which the time-dependent intensity signal can be normalized to derive time-dependent M_z/M_s data. Furthermore, the reference field sequences are applied at the beginning and the end of each measurement to verify whether the relevant intensity levels measured at the detector remain constant in time and we have stable experimental conditions (see Appendix for further details). The so-derived M_z/M_s signal scale is shown as the right-hand axis in Figs. 4(d) and 4(e). As can be easily seen, the reference saturation states align within $M_z/M_s = \pm 1$. Another relevant parameter for our analysis is the relative intensity change $\Delta I/I$, defined as

$$\frac{\Delta I}{I} = 2 \frac{\langle I_{\text{ref}}^+ \rangle - \langle I_{\text{ref}}^- \rangle}{\langle I_{\text{ref}}^+ \rangle + \langle I_{\text{ref}}^- \rangle}, \quad (9)$$

which is proportional to the effective light polarization changes upon the inversion of the magnetization and is thus proportional to M_z under otherwise stable experimental conditions.

In Fig. 4(b), the field amplitude in the central portion of the measurement is $H_0 = 457$ Oe, and for this case, a squarelike intensity signal is detected that is nearly identical to the reference measurements, as shown in Fig. 4(d). This observation means that this specific magnetic-field amplitude is still sufficiently large to induce full magnetization reversal at the chosen field frequency. As the magnetization oscillates between $\pm M_s$, the cycle-averaged magnetization is $Q_z = 0$, as illustrated by the green dashed lines, which means that the sample is in the dynamic PM phase. In Fig. 4(c) the field amplitude of the central measurement sequence portion is $H_0 = 281$ Oe. For this field amplitude, the measured intensity shown in Fig. 4(e) remains basically constant in contrast to the reference signal segments, and specifically, its value remains close to the magnetization saturation state set by the orientation of the magnetic field in the last half-period of the reference sequence. Thus, for the selected period P , this field amplitude H_0 is below the DPT, and $Q_z \neq 0$ in

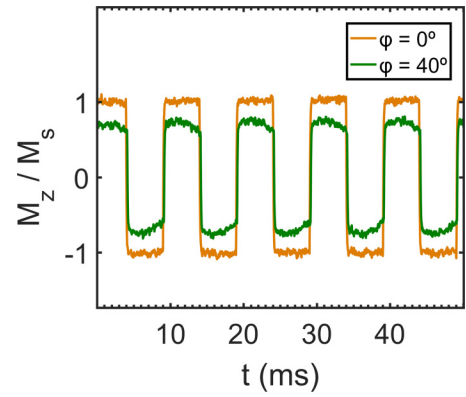


FIG. 5. Time-dependent magnetization signals measured for the $\text{Co}_{82}\text{Ru}_{18}$ sample and two different values of φ in between EA and the z axis for the same externally applied magnetic-field sequence with $H_0 = 581$ Oe and $P = 10$ ms.

accordance to the phase diagram in Fig. 1(e), representing the dynamic FM phase. Furthermore, we can conclude that the DPT lies between $H_0 = 281$ and 457 Oe, given the observed fundamental change in the dynamic magnetic response for this sample and the applied field frequency and orientation conditions employed. Thus we are in a position to access the DPT experimentally by varying H_0 while leaving the rest of the experimental parameters constant. These initial examples also demonstrate that our experimental setup allows us to measure the dynamic order parameter Q with very high sensitivity, even for individual field loops, so that also all derived quantities, such as susceptibility and fluctuation, can be precisely measured.

For different orientations of the samples, the reference signals need to be compared to the $\varphi = 0^\circ$ case, because only in this scenario can one associate the measured signal trace and thus the corresponding M_z values to M_s exactly. Thus time-dependent magnetization signals will always be normalized to the relative intensity change measured at $\varphi = 0^\circ$ (see Appendix for further details). In Fig. 5 we show two normalized magnetization signals ($\varphi = 0^\circ$ and $\varphi = 40^\circ$) for the $\text{Co}_{82}\text{Ru}_{18}$ sample and for a field amplitude of $H_0 = 581$ Oe. In both cases a similar time-dependent signal is measured. However, the maximum magnetization values that are dynamically accessed in the $\varphi = 40^\circ$ case are significantly smaller than in the EA-aligned case ($\varphi = 0^\circ$), which is also associated with a smaller relative intensity change according to Eq. (9). Thus for the frequencies and field amplitudes used in our study, magnetization values do not necessarily saturate along the z axis. Another noticeable effect are the small magnetization variations within each half period of the magnetization signal, which are due to the already mentioned magnetization rotations around the EA as the external field varies. These aspects of our experimental observations and the underlying physics are discussed in detail in Sec. III, but they are mentioned here to highlight the excellent sensitivity of our setup, even for cases in which magnetic field and EA are far from being aligned.

As explained in the Introduction, H_0 scans allow for a broader exploration of the phase space in the vicinity of the DPT for the case of slow critical dynamics, which is the

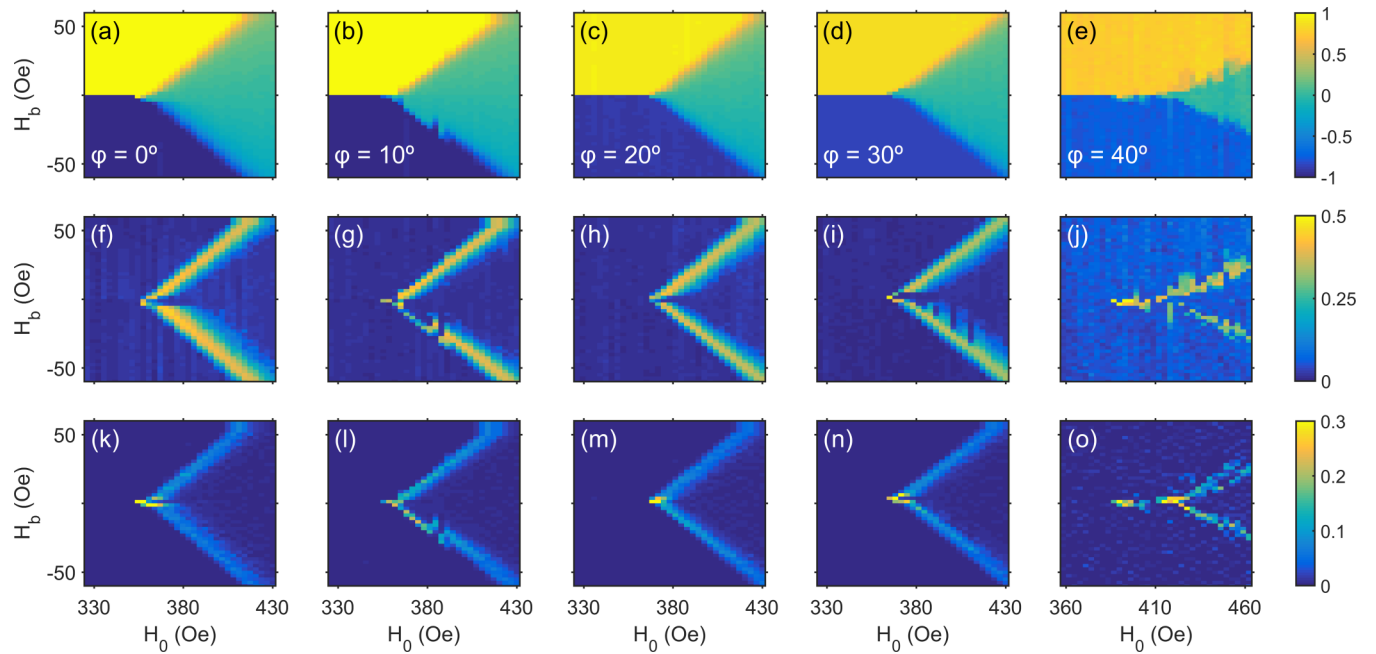


FIG. 6. Color-coded maps representing key experimental data in the $H_0 - H_b$ phase space close to the critical point for the Co sample using $P = 10$ ms and different values of φ : (a)–(e) show $\langle Q_z \rangle$ for the values of φ indicated in the subfigures, (f)–(j) show the corresponding fluctuations σ_{zz}^Q , and (k)–(o) the corresponding susceptibility χ_{zz}^Q data. The color-code bars for $\langle Q_z \rangle$, σ_{zz}^Q , and χ_{zz}^Q are shown on the right of (e), (j), and (o), respectively, and apply for all color maps within each row.

regime of our experiments. Thus we are utilizing H_0 scans here in conjunction with varying H_b to explore the entire phase space. Specifically, the following procedure has been applied for all our measurements. Light intensity data representing the dynamic magnetization information are collected while a series of magnetic-field signals are applied along the z axis. In our applied magnetic-field sequences, P is left constant while H_0 and H_b are swept in the vicinity of the critical point. For every individual H_0 value, H_b is stepwise decreased and subsequently increased after every 100 field oscillation periods in steps of 1.2 Oe. By doing this we can track the bistability regime of Q as a function of H_b in the dynamic FM phase, in addition to exploring the entire relevant phase space. This H_b sweep process is repeated five times for a single H_0 value [53]. Before and after every H_b sweep, five reference periods with a field amplitude of 581 Oe and $H_b = 0$ Oe are applied which serve as the reference measurements as explained above. After repeating said sequence, the H_0 value is systematically changed in steps of 4 Oe. The specific H_0 range that is measured is chosen in each case in such a way that both the FM and PM regimes are accessible for each φ value and selected frequency. For each (H_0, H_b) point within the explored phase space, 500 values of Q_z are obtained. From these Q_z data, $\langle Q_z \rangle$, σ_{zz}^Q , and χ_{zz}^Q are calculated following Eqs. (7) and (8). Further technical details of the data analysis can be found in the Appendix.

III. RESULTS AND DISCUSSION

The phase space in the vicinity of the DPT has been experimentally investigated following the previously mentioned

procedure for sample orientation angles φ ranging from -40° to 40° . In Fig. 6, color-coded maps show key experimental quantities measured for the Co sample as a function of both H_0 and H_b , and as such they represent this sample's dynamic order behavior in the vicinity of the DPT for $P = 10$ ms and several exemplary values of φ . The first row [Figs. 6(a)–6(e)] shows the results of $\langle Q_z \rangle$. The second row [Figs. 6(f)–6(j)] shows the corresponding results of σ_{zz}^Q , and the last row [Figs. 6(k)–6(o)] displays the associated values for χ_{zz}^Q . The color bars corresponding to the three different quantities shown in Fig. 6 are visible on the right-hand side of Figs. 6(e), 6(j), and 6(o), respectively, and are valid for each entire row of data maps. Figure 6(a) specifically shows the dynamically stable states of $\langle Q_z \rangle$ for the Co sample and $\varphi = 0^\circ$. Here, below a critical field amplitude of $H_0^{\text{crit}} = 350$ Oe, two distinct regions are visible as yellow and blue parts, which correspond to dynamic states in which $\langle Q_z \rangle$ is significantly different from zero and actually reaches values close to saturation, i.e., $\langle Q_z \rangle \approx \pm 1$. These regions represent the two equivalent but sign-inverted stable states of the dynamic FM phase. Above the critical field amplitude H_0^{crit} there is a fundamental change in the dynamic behavior and now along the $H_b = 0$ Oe line, $\langle Q_z \rangle = 0$, which is represented by the green color in the map. This distinct change in $\langle Q_z \rangle$ corroborates that the DPT happens at H_0^{crit} , thereby clearly dividing the FM and PM phases. In the PM phase ($H_0 > H_0^{\text{crit}}$), $\langle Q_z \rangle$ changes continuously upon increasing and decreasing H_b , even if there are regions where the $\langle Q_z \rangle$ vs H_b dependence becomes very steep, which appear as the green-to-yellow and green-to-blue transition regions, analogous to earlier experimental observations for the dynamic PM phase [22]. Figures 6(f) and 6(k) show the corresponding experimental data for σ_{zz}^Q and χ_{zz}^Q , respectively.

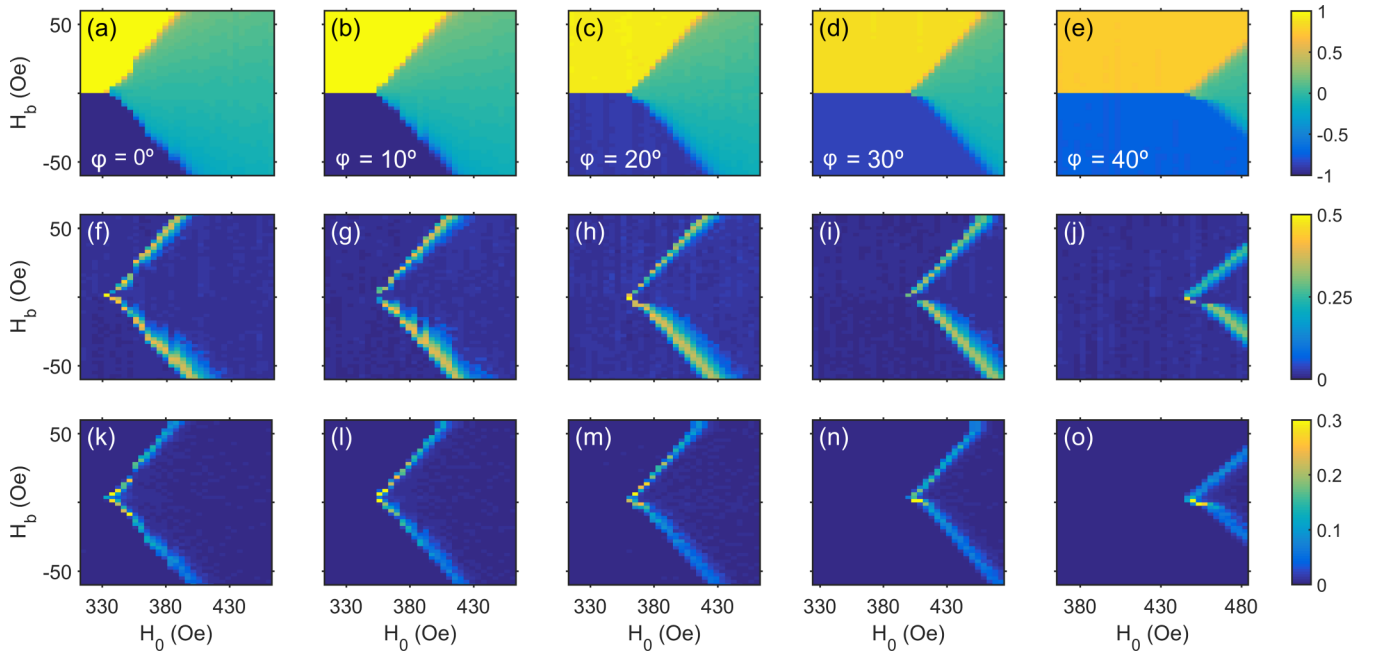


FIG. 7. Color-coded maps representing key experimental data in the $H_0 - H_b$ phase space close to the critical point for the $\text{Co}_{82}\text{Ru}_{18}$ sample using $P = 10$ ms and different values of φ : (a)–(e) show $\langle Q_z \rangle$ for the values of φ indicated in the subfigures, (f)–(j) show the corresponding fluctuations σ_{zz}^Q , and (k)–(o) the corresponding susceptibility χ_{zz}^Q data. The color-code bars for $\langle Q_z \rangle$, σ_{zz}^Q , and χ_{zz}^Q are shown on the right of (e), (j), and (o), respectively, and apply for all color maps within each row.

Both maps identify large values of their respective quantities above H_0^{crit} in a band-type geometry which coincides with the steep changes of $\langle Q_z \rangle$ vs H_b . These features of the dynamic PM state are so-called metamagnetic anomalies, and our observations here agree well with the results in Ref. [22], where these anomalous fluctuations were first reported. The main difference is a technical one in that here the phase space is being explored by varying H_0 for a constant P , whereas in [22] P was varied and H_0 held constant. It is nonetheless important to notice that despite this experimental change, the metamagnetic fluctuations can still be clearly observed in the PM phase space, even in this wide-range exploration of the phase space that is being facilitated by means of the H_0 scan according to Fig. 1(e).

Figures 6(b)–6(e) show color-coded maps of $\langle Q_z \rangle$ within the explored phase space for different orientations of the EA with respect to the applied field. We observe that the appearance of $\langle Q_z \rangle$ within each respective phase-space segment is rather similar in all the cases. Two different FM regimes as well as the PM phase are clearly visible and identifiable by their respective color similarly to the $\varphi = 0^\circ$ case, and the FM and PM phases are separated by the corresponding critical points at specific and φ -dependent H_0^{crit} values. Also, within each dynamic phase we find very similar order-parameter dependencies as a function of the phase-space position (H_0, H_b). From these data we can conclude that the DPT is clearly existent in all cases, and the phase space does not change in any qualitatively significant manner as a function of φ . Figures 6(g)–6(j) show the corresponding maps of σ_{zz}^Q and Figs. 6(l)–6(o) the associated data for χ_{zz}^Q , each for a different value of φ . In all these plots, metamagnetic anomalies are clearly observable in the dynamic PM phase, and the overall

shape of where they occur is similar for all values of φ investigated here. This experimental observation leads us to the first main conclusion of our work, namely, that the fundamental occurrence and properties of the DPT are not significantly affected by a misalignment in between the EA of a uniaxial magnetic system and the direction of the applied field.

There are, however, noticeable differences between the data sets for different field orientations. In the $\langle Q_z \rangle$ maps [Figs. 6(b)–6(e)] we observe a relevant decrease in the contrast between the two dynamically ordered states ($H_0 < H_0^{\text{crit}}$) as φ increases. The values of $\langle Q_z \rangle$ associated with the two stable states in the FM phase monotonously decrease as φ increases. This decrease can be explained by the fact that the field amplitudes required for the observation of the DPT are significantly lower than the anisotropy field H_k of the sample, as already indicated in conjunction with our discussion of Figs. 3(d) and 3(e). Therefore rotations of the magnetization vector \mathbf{M} away from the EA and towards the applied field direction are only modest in size, even for $\varphi = 40^\circ$, and accordingly, the experimentally detected magnetization component M_z for these dynamically stable FM states is very similar to the z -axis projection of an EA-aligned magnetization vector. It is also noticeable that the numerical value of the critical point H_0^{crit} increases with φ . This effect can be explained by the nucleation of reversal domains [15], which we will discuss in detail in conjunction with Figs. 8 and 9.

In Fig. 7, the same types of results are shown for the $\text{Co}_{82}\text{Ru}_{18}$ sample. The maps in Figs. 7(a)–7(e) show the $\langle Q_z \rangle$ data as a function of the phase-space position (H_0, H_b) for five different angular orientations in the range of $\varphi = 0^\circ$ – 40° . Figures 7(f)–7(j) show the corresponding results for σ_{zz}^Q and Figs. 7(k)–7(o) the associated data for χ_{zz}^Q . Specifically, we

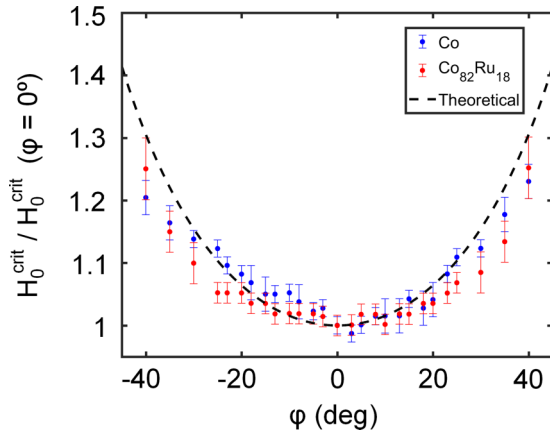


FIG. 8. $H_0^{\text{crit}}/H_0^{\text{crit}}(\varphi = 0^\circ)$ vs φ for the Co (blue) and $\text{Co}_{82}\text{Ru}_{18}$ (red) samples. The black dashed line follows the theoretical model in [56].

can see that when EA and the applied field are parallel, i.e., $\varphi = 0^\circ$, the color-coded map of $\langle Q_z \rangle$ in Fig. 7(a) is extremely similar to the case of the pure Co sample seen in Fig. 6(a). This implies that the different T_C values of the two samples, and consequently, the different T/T_C ratios at which our room-temperature measurements were carried out, are not significantly affecting the overall qualitative behavior of the DPT and the underlying processes of magnetization reversal [39]. Thus, also for the $\text{Co}_{82}\text{Ru}_{18}$ sample metamagnetic anomalies are clearly visible in Figs. 7(f) and 7(k), which furthermore exhibit a similar pattern as in Figs. 6(f) and 6(k), respectively. Regarding the measurements at different sample orientations, the results for $\langle Q_z \rangle$ in Figs. 7(b)–7(e) for the $\text{Co}_{82}\text{Ru}_{18}$ sample also show a similar behavior to those presented in Figs. 6(b)–6(e) for the pure Co sample. In both cases the decrease of $\langle Q_z \rangle$ in the FM phase is noticeable as φ increases. At the same time we also identify an increase of H_0^{crit} for increasing values of φ . With all this we can conclude that the DPT and the phase space in its vicinity does not significantly change upon rotating the EA away from the direction of the field. The value of $\langle Q_z \rangle$ is dominated by the magnetization being aligned with the EA. Furthermore, we can identify a virtually identical behavior in the two different samples, even if the T/T_C ratio of the $\text{Co}_{82}\text{Ru}_{18}$ sample is significantly larger than that of the Co sample, as explained in Sec. II. It should also be noticed that the fluctuation data in Figs. 7(g)–7(j) exhibit a slight experimental asymmetry with respect to the $H_b = 0$ Oe line. This asymmetry is an experimental feature due to small field misalignments that do not perturb the overall behavior of the DPT in a very significant way. Furthermore, it is important to add that our experimental results for negative angles, which are not displayed in Figs. 6 and 7, show an overall symmetric behavior with respect to the EA case data for both our samples.

As we already pointed out, there is the shift of the critical point H_0^{crit} towards larger H_0 values as φ increases, a fact that we observe for both samples. To further illustrate this, we show in Fig. 8 the measured values of H_0^{crit} normalized to its value at $\varphi = 0^\circ$ for both samples. The clear increase of the critical field with $|\varphi|$ implies that larger field amplitudes

are required to trigger the microscopic magnetization reversal processes and the associated DPT. In the context of uniaxial ferromagnets at ambient temperature, the process of magnetization reversal is initiated by the thermal nucleation of reversal domains [15,24,42,54,55]. In this regime, droplets of inverted magnetization states (in reference to the background magnetization) are thermally activated and can subsequently expand if they lower the Zeeman energy term in Eq. (5) once a certain energy barrier is surpassed. We have compared our results with the simple model described by Kondorsky [56,57] in which the field required for the magnetization reversal follows a $1/\cos(\varphi)$ angular dependency. This particular angular dependency is hereby the result of the competition of the additional domain-wall energy of a nucleated reversal domain with its gain in Zeeman energy. While the domain-wall energy can be assumed to be field orientation independent, the Zeeman energy gained is proportional to $M_s H_0 \cos(\varphi)$ under the assumption that the magnetization is aligned along the EA, and thus coherent rotations are not significant to initiate the process of magnetization reversal. To compensate for the loss of effectiveness of the applied field upon rotating the EA away from the field axis by an angle φ , H_0 has to be increased by a factor of $1/\cos(\varphi)$ to reestablish the energy balance for reversal nucleation to occur. This simple model, shown as a black dashed line in Fig. 8, agrees fairly well with our experimental data, which underscores that the magnetization reversal onset in our samples is governed by reversal domain nucleation. Furthermore, this observation also corroborates the already mentioned fact that the magnetization rotation levels that we do detect in our measurements, as shown in Fig. 5, represent a rather small effect for the field strength and frequencies used in our study.

For the $\text{Co}_{82}\text{Ru}_{18}$ sample, for instance, the rotation-induced magnetization changes are found to account for only up to 7% of the full magnetization reversal amplitude for a field strength of $H_0 = 581$ Oe (see Fig. 5), and for the Co sample, these changes are even smaller, staying below 5% for the same field amplitude and a field orientation of $\varphi = 40^\circ$. These observations also agree with the fact that in our measurements the DPT happens at field amplitudes that are much lower than H_k , and therefore only very modest magnetization rotations away from the EA occur. Correspondingly, the dynamic magnetization states remain closely aligned along the EA under all experimental conditions and only small oscillations around the EA can develop, as shown in Figs. 3(d) and 3(e). This interpretation of our data implies that as φ deviates from 0° , \mathbf{Q} will develop an x component in the dynamic FM phase, while the z component is successively reduced upon increasing the absolute value of φ . Specifically, if \mathbf{M} were to remain perfectly aligned with the EA, the φ dependence of \mathbf{Q} should follow a $\mathbf{Q} = Q_0[\sin(\varphi), 0, \cos(\varphi)]$ vector trajectory, at least approximately, where Q_0 represents the value of the order parameter along the EA. Given that our experimental signal is proportional to Q_z or M_z , we have analyzed our experimental data to verify the assumed \mathbf{Q} vs φ dependence. Hereby, the $\Delta I/I$ values that we defined in Eq. (9) are actually providing the most reliable data. In Fig. 9 we show the relative intensity change between inverted magnetization states for different angular orientations of both samples and find that the $\Delta I/I$ value reaches its maximum at $\varphi = 0^\circ$ and decreases as $|\varphi|$ increases.

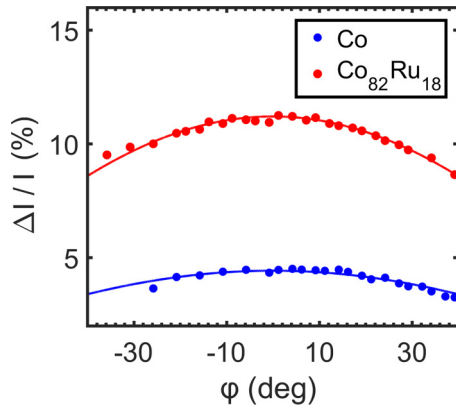


FIG. 9. Relative intensity change upon magnetization reversal vs sample orientation angle φ for the Co (blue) and $\text{Co}_{82}\text{Ru}_{18}$ (red) samples. The solid lines represent the corresponding least-squares fits to a cos function describing the response of magnetization being parallel to the EA at all times.

The quality of the fits to the $\cos(\varphi)$ curve is excellent and fully agrees with the fact that the magnetization vector aligns closely with the EA at all times. Experimentally, this also agrees fully with the observed decrease in the values of $\langle Q_z \rangle$ in the FM phase, which were already mentioned in conjunction with Figs. 6(b)–6(e) and 7(b)–7(e), allowing us to corroborate the $\mathbf{Q} = Q_0[\sin(\varphi), 0, \cos(\varphi)]$ vector trajectory.

From the data in Figs. 6 and 7, it is also evident that metamagnetic anomalies are existent in the PM phase for all angles φ investigated. However, this data representation does not allow us to analyze if the anomalies show any specific φ dependency. Correspondingly, we have carried out a quantitative analysis of the magnitude of the anomalous metamagnetic fluctuations in order to compare the behavior for different values of φ and to gain further insight about the tensorial nature of σ^Q . More specifically, we are interested in the possible influence of magnetization rotations onto σ_{zz}^Q as φ increases. To facilitate this analysis, one has to keep in mind that the values of σ_{zz}^Q may be significantly reduced upon increasing φ , given that $\langle Q_z \rangle$ is itself reduced as one increases φ . In order to properly quantify the magnitude of metamagnetic anomalies and analyze the possible impact of magnetization rotations, we have calculated for each orientation angle φ the probability density histograms $P(\sigma_{zz}^Q/\langle Q_z \rangle, \varphi)$ of normalized fluctuation sizes $\sigma_{zz}^Q/\langle Q_z \rangle$ in a constant phase-space segment close to the critical point. The selected phase-space window is $H_0 \in [H_0^{\text{crit}}, 1.12H_0^{\text{crit}}]$ and $|H_b| < 0.09H_0^{\text{crit}}$. Figure 10 shows the ratio η of the probability to observe very large fluctuations $\sigma_{zz}^Q/\langle Q_z \rangle > 0.1$ normalized to its value at $\varphi = 0^\circ$, i.e.,

$$\eta = \frac{P(\sigma_{zz}^Q/\langle Q_z \rangle > 0.1, \varphi)}{P(\sigma_{zz}^Q/\langle Q_z \rangle > 0.1, \varphi = 0^\circ)}. \quad (10)$$

For both samples, η remains close to 1 for small absolute values of φ . This means that for the selected phase-space window the probability of large fluctuations $\sigma_{zz}^Q/\langle Q_z \rangle > 0.1$ that are associated with strong metamagnetic anomalies is similar for these values of φ . In particular, for the Co sample we do not observe any significant change of η vs φ in the entire range that we have explored, which is fully consistent with the previously drawn conclusion that the behavior is clearly

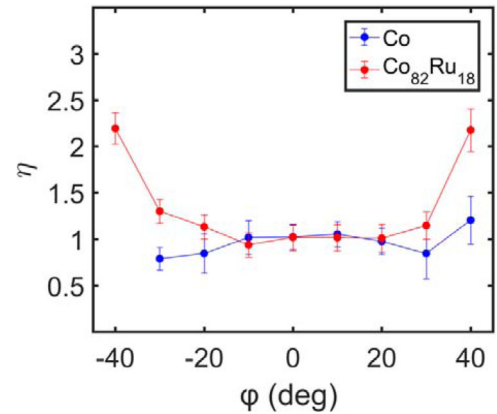


FIG. 10. Probability to find $\sigma_{zz}^Q/\langle Q_z \rangle > 0.1$ as a function of φ , normalized to the corresponding value at $\varphi = 0^\circ$ for the Co (blue) and $\text{Co}_{82}\text{Ru}_{18}$ (red) samples.

dominated by a near perfect EA alignment of the magnetization throughout the dynamic magnetic state. However, for the $\text{Co}_{82}\text{Ru}_{18}$ sample, which represents a much higher T/T_C ratio, we do observe a significant increase of η with φ for the largest EA to field misalignments, i.e., $|\varphi| = 40^\circ$. The fact that the strength of the metamagnetic tendencies increases with φ only for the Ru-doped sample could be associated with the somewhat smaller anisotropy in this structure, which yields slightly larger magnetization rotations. Furthermore, this sample also has a lower T_C and thus can exhibit thermal fluctuation more easily, a fact that is by itself of course independent of φ . However, it might be the conjunction of both of these facts, i.e., the larger rotation values in the presence of enhanced thermal fluctuations that could trigger larger metamagnetic fluctuations as φ increases for the $\text{Co}_{82}\text{Ru}_{18}$ sample. It is worthwhile to mention, though, that this φ dependency does not significantly affect the general qualitative behavior of the dynamic order parameter \mathbf{Q} and associated quantities in the phase space close to the DPT.

IV. CONCLUSIONS AND OUTLOOK

In this work we have experimentally studied the dynamic magnetic behavior in the phase space surrounding the DPT for anisotropic ferromagnets with in-plane magnetization as a function of the orientation in between the EA and the applied field direction to enable a first assessment of the vector nature of \mathbf{Q} , i.e., the macroscopic dynamic order parameter, which defines the DPT and classifies its associated phase space. Based upon this work, several relevant conclusions can be drawn.

First, for different orientations of the EA with respect to the field direction we find the phase diagram not to be significantly impacted in terms of its qualitative behavior. The existence of the DPT is clearly observable for both samples, representing different T/T_C ratios, and in all the experimental data, the Q component parallel to the field, as well as the dynamic fluctuation and susceptibility tensor components, show very similar behavior and fundamentally identical characteristics in the vicinity of the critical point. The occurrence of metamagnetic anomalies in the dynamic PM phase is also

observable in all cases, verifying a qualitatively identical behavior of Q_z for the different values of φ . In this context it is relevant to notice that magnetization reversal is initiated by domain nucleation for all values of φ and is furthermore triggered by field amplitudes which are much lower than each sample's anisotropy field. This explains why magnetization rotations are a second-order effect, and throughout entire dynamic sequences the magnetization remains closely aligned with the EA.

For the specific parameter range and samples used in this study, we can conclude that the vectorial nature of \mathbf{Q} is only associated with a rather trivial rotation of \mathbf{Q} in the x - z plane, given the dominance of EA magnetization alignment throughout each dynamic cycle anywhere in the phase diagram. Thus the entirety of the dynamic phase space explored is primarily driven by the components of the magnetic fields H_0 and H_b that are parallel to the EA. It would be very interesting to explore dynamic phase transitions in the regime where H_0 and H_k are more comparable in size, at which point magnetization rotations should be significant and easily tunable via the field alignment angle φ . In this regime more significant phase diagram modifications should be expected. However, experimentally this would require uniform magnetic fields at frequencies in the tens to hundreds of megahertz, which is beyond available experimental capabilities, especially with respect to real-time magnetization detection sensitivity. Another extension of experimental work that would be useful for further explorations is full vector magnetometry to enable the simultaneous detection of the various \mathbf{Q} vector components describing the system-averaged dynamic state. This is even possible by means of magneto-optical measurements, for which vector magnetometry has been demonstrated [58,59]. Lastly, it would be interesting to compare our present experimental results with theoretical studies in the context of the anisotropic Heisenberg model, as well as utilize such models to explore the vector nature of \mathbf{Q} in further detail, given that also in theoretical works to date, the vector nature of \mathbf{Q} has been mostly ignored.

ACKNOWLEDGMENTS

Work at nanoGUNE was supported by the Spanish Ministry of Science and Innovation under the Maria de Maeztu Units of Excellence Programme (Grant No. MDM-2016-0618) and Project No. RTI2018-094881-B-100 (MCIU/Feder), as well as by predoctoral fellowship No. PRE2019-088428. J.M.M.R. acknowledges Colciencias for his PhD fellowship.

APPENDIX

In our experimental setup the magnetic-field value is measured by means of a Hall sensor inside the gap of the electromagnet. The amplitude H_0 and bias H_b are obtained by analyzing the magnetic-field components via a fast Fourier transform (FFT) analysis of the signal. The light intensity signal processing works as follows. Reference intensity values $\langle I_{\text{ref}}^+ \rangle$ and $\langle I_{\text{ref}}^- \rangle$ are taken by averaging the intensity values measured in each half period of the reference signal. We also define $\langle I_{\text{ref}} \rangle$ as the average intensity measured for the reference

sequence. It is worth mentioning that the points measured in the magnetization reversal region are not taken into account to minimize error sources. In principle, laser instabilities could yield time-dependent intensity drifts of the complete signal. The drift, if it exists, is envisioned to be linear, so we apply a linear compensation by determining the slope in between the two reference value determinations (for each $\pm M_s$ saturation state), one prior to and one after the actual dynamic magnetization measurement. Overall, we find the signal drift to be vanishingly small in comparison to the detector noise due to the quality of the laser that we used, as well as the mechanical stability of our setup. After formally compensating for the linear drift, we calculate both absolute intensity change ΔI and the relative intensity change $\Delta I/I$ as

$$\Delta I = \langle I_{\text{ref}}^+ \rangle - \langle I_{\text{ref}}^- \rangle, \quad (\text{A1})$$

$$\frac{\Delta I}{I} = 2 \frac{\langle I_{\text{ref}}^+ \rangle - \langle I_{\text{ref}}^- \rangle}{\langle I_{\text{ref}}^+ \rangle + \langle I_{\text{ref}}^- \rangle}. \quad (\text{A2})$$

The data sampling frequency is $f_s = 30$ kHz, i.e., we measure $N_s = 300$ points per period oscillation. The discrete time intensity signal is I_{ij} , which refers to the j th point of the i th field oscillation, from which we calculate the individual magnetization values as

$$\frac{M_{zij}}{M_s} = 2 \frac{I_{ij} - \langle I_{\text{ref}} \rangle}{\Delta I} \frac{\Delta I/I(\varphi)}{\Delta I/I(\varphi = 0^\circ)}. \quad (\text{A3})$$

For each period we calculate a single value of the order parameter Q_{zi} ,

$$Q_{zi} = \frac{1}{N_s} \sum_{j=1}^{N_s} \frac{M_{zij}}{M_s}, \quad (\text{A4})$$

where M_{zij} is the j th magnetization point of the i th field oscillation. We measure a total of $N = 500$ periods for each (H_0, H_b) phase-space point, from which we determine $\langle Q_z \rangle$, $\langle Q_z^2 \rangle$, and σ_{zz}^Q as

$$\langle Q_z \rangle = \frac{1}{N} \sum_{i=1}^N Q_{zi}, \quad (\text{A5})$$

$$\langle Q_z^2 \rangle = \frac{1}{N} \sum_{i=1}^N Q_{zi}^2, \quad (\text{A6})$$

$$\sigma_{zz}^Q = \sqrt{\langle Q_z^2 \rangle - \langle Q_z \rangle^2}. \quad (\text{A7})$$

At the same time, susceptibility values are obtained by calculating the discrete derivative of $\langle Q_z \rangle$ as a function of H_b for constant H_0 :

$$\begin{aligned} \chi_{zz}^Q(H_0, H_b + 1/2 \Delta H_b) \\ = \frac{\langle Q_z \rangle(H_0, H_b + \Delta H_b) - \langle Q_z \rangle(H_0, H_b)}{\Delta H_b}. \end{aligned} \quad (\text{A8})$$

Notice that this expression applies only for this tensor component of the dynamic susceptibility and having the applied field components H_0 and H_b along the z axis following $\mathbf{H} = H(t)(0, 0, 1)$ with $H(t) = H_0 \cos(2\pi t/P) + H_b$.

- [1] M. C. Cross and P. C. Hohenberg, *Rev. Mod. Phys.* **65**, 851 (1993).
- [2] J. Kröll, J. Darmo, S. S. Dhillon, X. Marcadet, M. Calligaro, C. Sirtori, and K. Unterrainer, *Nature (London)* **449**, 698 (2007).
- [3] A. Shekhawat, S. Zapperi, and J. P. Sethna, *Phys. Rev. Lett.* **110**, 185505 (2013).
- [4] D. Bonamy, S. Santucci, and L. Ponsou, *Phys. Rev. Lett.* **101**, 045501 (2008).
- [5] J. L. Hansen, M. van Hecke, A. Haaning, C. Ellegaard, K. H. Andersen, T. Bohr, and T. Sams, *Nature (London)* **410**, 324 (2001).
- [6] G. W. Baxter, R. P. Behringer, T. Fagert, and G. A. Johnson, *Phys. Rev. Lett.* **62**, 2825 (1989).
- [7] V. K. Jirsa and H. Haken, *Phys. Rev. Lett.* **77**, 960 (1996).
- [8] I. Shmulevich, S. A. Kauffman, and M. Aldana, *Proc. Natl. Acad. Sci. USA* **102**, 13439 (2005).
- [9] P. Bak, C. Tang, and K. Wiesenfeld, *Phys. Rev. A* **38**, 364 (1988).
- [10] T. Tome and M. J. de Oliveira, *Phys. Rev. A* **41**, 4251 (1990).
- [11] Usually in the framework of Monte Carlo simulations, square magnetic field signals are considered. Experimental studies usually employ sinusoidal signals.
- [12] R. J. Glauber, *J. Math. Phys.* **4**, 294 (1963).
- [13] P. Riego, P. Vavassori, and A. Berger, *Physica B*, **549**, 13 (2018).
- [14] S. W. Sides, P. A. Rikvold, and M. A. Novotny, *Phys. Rev. E* **59**, 2710 (1999).
- [15] G. Korniss, C. J. White, P. A. Rikvold, and M. A. Novotny, *Phys. Rev. E* **63**, 016120 (2000).
- [16] H. Fujisaka, H. Tutu, and P. A. Rikvold, *Phys. Rev. E* **63**, 036109 (2001).
- [17] S. W. Sides, P. A. Rikvold, and M. A. Novotny, *Phys. Rev. Lett.* **81**, 834 (1998).
- [18] D. T. Robb, P. A. Rikvold, A. Berger, and M. A. Novotny, *Phys. Rev. E* **76**, 021124 (2007).
- [19] R. A. Gallardo, O. Idigoras, P. Landeros, and A. Berger, *Phys. Rev. E* **86**, 051101 (2012).
- [20] O. Idigoras, P. Vavassori, and A. Berger, *Physica B* **407**, 1377 (2012).
- [21] D. T. Robb and A. Ostrander, *Phys. Rev. E* **89**, 022114 (2014).
- [22] P. Riego, P. Vavassori, and A. Berger, *Phys. Rev. Lett.* **118**, 117202 (2017).
- [23] G. M. Buendía and P. A. Rikvold, *Phys. Rev. B* **96**, 134306 (2017).
- [24] See, for instance, A. Kirilyuk, J. Ferre, and D. Renard, *J. Magn. Mater.* **171**, 45 (1997).
- [25] M. Acharyya, *Phys. Rev. E* **56**, 1234 (1997).
- [26] H. Jang, M. J. Grimson, and C. K. Hall, *Phys. Rev. B* **67**, 094411 (2003).
- [27] P. Riego and A. Berger, *Phys. Rev. E* **91**, 062141 (2015).
- [28] M. Acharyya, *Phys. Rev. E* **69**, 027105 (2004).
- [29] Z. Huang, Z. Chen, F. Zhang, and Y. Du, *Phys. Lett. A* **338**, 485 (2005).
- [30] Y. L. He and G. C. Wang, *Phys. Rev. Lett.* **70**, 2336 (1993).
- [31] Q. Jiang, H. N. Yang, and G. C. Wang, *Phys. Rev. B* **52**, 14911 (1995).
- [32] J. S. Suen and J. L. Erskine, *Phys. Rev. Lett.* **78**, 3567 (1997).
- [33] D. T. Robb, Y. H. Xu, O. Hellwig, J. McCord, A. Berger, M. A. Novotny, and P. A. Rikvold, *Phys. Rev. B* **78**, 134422 (2008).
- [34] A. Berger, O. Idigoras, and P. Vavassori, *Phys. Rev. Lett.* **111**, 190602 (2013).
- [35] M. Bander and D. L. Mills, *Phys. Rev. B* **38**, 12015(R) (1988).
- [36] O. Idigoras, A. K. Suszka, P. Vavassori, B. Obry, B. Hillebrands, P. Landeros, and A. Berger, *J. Appl. Phys.* **115**, 083912 (2014).
- [37] O. Idigoras, U. Palomares, A. K. Suszka, L. Fallarino, and A. Berger, *Appl. Phys. Lett.* **103**, 102410 (2013).
- [38] B. J. Kirby, L. Fallarino, P. Riego, B. B. Maranville, C. W. Miller, and A. Berger, *Phys. Rev. B* **98**, 064404 (2018).
- [39] J. M. Marín Ramírez, E. Oblak, P. Riego, G. Campillo, J. Osorio, O. Arnache, and A. Berger, *Phys. Rev. E* **102**, 022804 (2020).
- [40] W. Yang, D. N. Lambeth, and D. E. Laughlin, *J. Appl. Phys.* **85**, 4723 (1999).
- [41] E. C. Stoner and E. P. Wohlfarth, *Philos. Trans. R. Soc. London* **240**, 599 (1948).
- [42] A. Misra and B. K. Chakrabarti, *Europhys. Lett.* **52**, 311 (2000).
- [43] P. Vavassori, *Appl. Phys. Lett.* **77**, 1605 (2000).
- [44] Z. Q. Qiu and S. D. Bader, *Rev. Sci. Instrum.* **71**, 1243 (2000).
- [45] O. V. Borovkova, H. Hashim, M. A. Kozhaev, S. A. Dagesyan, A. Chakravarty, M. Levy, and V. I. Belotelov, *Appl. Phys. Lett.* **112**, 063101 (2018).
- [46] T. Higo, H. Man, D. B. Gopman, L. Wu, T. Koretsune, O. M. J. van'T Erve, Y. P. Kabanov, D. Rees, Y. Li, M. T. Suzuki, S. Patankar, M. Ikhlas, C. L. Chien, R. Arita, R. D. Shull, J. Orenstein, and S. Nakatsuji, *Nat. Photonics* **12**, 73 (2018).
- [47] T. H. J. Loughran, P. S. Keatley, E. Hendry, W. L. Barnes, and R. J. Hicken, *Opt. Express* **26**, 4738 (2018).
- [48] E. R. Moog and S. D. Bader, *Superlattices Microstruct.* **1**, 543 (1985).
- [49] Z. Q. Qiu, J. Pearson, and S. D. Bader, *Phys. Rev. Lett.* **70**, 1006 (1993).
- [50] A. Berger, S. Knappmann, and H. P. Oepen, *J. Appl. Phys.* **75**, 5598 (1994).
- [51] E. Oblak, P. Riego, L. Fallarino, A. Martínez-De-Guerenu, F. Arizti, and A. Berger, *J. Phys. D: Appl. Phys.* **50**, 23LT01 (2017).
- [52] E. Oblak, P. Riego, A. Garcia-Manso, A. Martínez-de-Guerenu, F. Arizti, I. Artetxe, and A. Berger, *J. Phys. D: Appl. Phys.* **53**, 205001 (2020).
- [53] The field stability is ensured by relaxing any possible transient behavior before each H sweep process.
- [54] P. A. Rikvold, H. Tomita, S. Miyashita, and S. W. Sides, *Phys. Rev. E* **49**, 5080 (1994).
- [55] G. Korniss, P. A. Rikvold, and M. A. Novotny, *Phys. Rev. E* **66**, 056127 (2002).
- [56] F. Schumacher, *J. Appl. Phys.* **69**, 2465 (1991).
- [57] M. Mathews, E. P. Houwman, H. Boschker, G. Rijnders, and D. H. A. Blank, *J. Appl. Phys.* **107**, 013904 (2010).
- [58] A. Berger and M. R. Pufall, *J. Appl. Phys.* **85**, 4583 (1999).
- [59] J. A. Arregi, J. B. González-Díaz, O. Idigoras, and A. Berger, *Phys. Rev. B* **92**, 184405 (2015).